Statistical analysis of mesospheric gravity waves over King Sejong Station, Antarctica (62.2°S, 58.8°W)

CrossMark

Hosik Kam[a], Geonhwa Jee[b], Yong Kim[a,*], Young-bae Ham[b], In-Sun Song[b]

[a] Department Astronomy, Space Science and Geology, Chungnam National University, Daejeon, South Korea
[b] Korea Polar Research Institute, Incheon, South Korea

ARTICLE INFO

ABSTRACT

We have investigated the characteristics of mesospheric short period (< 1 h) gravity waves which were observed with all-sky images of OH Meinel band and OI 557 nm airglows over King Sejong Station (KSS) (62.22°S, 58.78°W) during a period of 2008–2015. By applying 2-dimensional FFT to time differenced images, we derived horizontal wavelengths, phase speeds, and propagating directions (188 and 173 quasi-monochromatic waves from OH and OI airglow images, respectively). The majority of the observed waves propagated predominantly westward, implying that eastward waves were filtered out by strong eastward stratospheric winds. In order to obtain the intrinsic properties of the observed waves, we utilized winds simultaneously measured by KSS Meteor Radar and temperatures from Aura Microwave Limb Sounder (MLS). More than half the waves propagated horizontally, as waves were in Doppler duct or evanescent in the vertical direction. This might be due to strong eastward background wind field in the mesosphere over KSS. For freely propagating waves, the vertical wavelengths were in the interquartile range of 9–33 km with a median value of 15 km. The vertical wavelengths are shorter than those observed at Halley station (76°S, 27°W) where the majority of the observed waves were freely propagating. The difference in the wave propagating characteristics between KSS and Halley station suggests that gravity waves may affect mesospheric dynamics in this part of the Antarctic Peninsula more strongly than over the Antarctic continent. Furthermore, strong wind shear over KSS played an important role in changing the vertical wavenumbers as the waves propagated upward between two airglow layers (87 and 96 km).

1. Introduction

The short period (< 1 h) gravity waves (GWs) play an important role in the global meridional circulation and alter the temperature structure of mesosphere and lower thermosphere (MLT) region (Fritts and Alexander, 2003). It has been shown that as much as 70% of the momentum transported into the MLT region is due to short-period GWs penetrating into this region from below (Fritts and Vincent, 1987). The spatial and temporal morphology of mesospheric GWs are important to understand the dynamics of the MLT region (Smith, 2004). Therefore, many studies have devoted to address the climatologic pattern of upwardly propagating GWs (e.g. Krassovski, 1972; Gavrilov and Shved, 1982; Swenson and Mende, 1994; Taylor et al., 1987; Taylor et al., 1995a; Gavrilov et al., 2002).

Phenomena of GWs in MLT region are mainly studied using ground based observations of the airglow, such as scanning photometers, spectral airglow temperature imagers and all-sky imagers (e.g. Taylor et al., 1995b). Satellite observations also provided the global climato-

logic pattern of GWs in the upper atmosphere (Wu and Jiang, 2002; Alexander et al., 2008; Wu and Eckermann, 2008; Ern et al., 2004). The Antarctic Peninsula has been noted as a global hot spot of GWs by Cryogenic Infrared Spectrometers and Telescopes (CRISTA) on board Shuttle Pallet Satellite (SPAS) and Upper Atmosphere Research Satellite Microwave Limb Sounder (UARS MLS) (Jiang et al., 2003; Ern et al., 2004). Interaction of surface winds with sharped edge topography of the Peninsula is considered as the source of the GW hotspot (Baumgaerter and McDonald, 2007; Alexander et al., 2007; Hertzog et al., 2008; Plougonven et al., 2008). In addition, the wave activity enhancement has been related to its proximity of Southern polar vortex (Yoshiki et al., 2004; Moffat-Griffin et al., 2011). Espy et al. (2006) reported that the magnitude of mesospheric GWs momentum flux over Rothera station (67°S, 68°W), located at the Antarctic Peninsula, was about 4 times larger than those of Halley station (76°S, 27°W) in the Antarctic plateau. Lee et al. (2013) analyzed wind data measured by a meteor radar at King Sejong Station (hereafter KSS, 62.22°S, 58.78°W), located further north near the tip of the

Antarctic Peninsula, and found wind variances, as a proxy of GW activity, even larger than those of Rothera station.

Although there have been studies of GW with all-sky airglow imagers at high latitudes (Bageston el al, 2009; Espy et al., 2004; Nielsen et al., 2009), all-sky imaging data are still in need for climatology studies. This need is evident at the tip of the Antarctic Peninsula, where, despite the recognized hotspot of GW activity, the weather condition is not favorable for imaging observation due to the persistent low pressure system. In this paper, we analyzed eight year observation data of all-sky images at KSS to derive the statistical characteristics of the short-period GWs in the mesosphere over the GW hotspot.

2. Observation and methodology

Korea Polar Research Institute (KOPRI) has been operating an all-sky camera at KSS since 2008. The all-sky camera consists of a 180° FOV lens (24 mm/F4.0) with telecentric optics for a multi-wavelength filter system and a liquid-cooled back-illuminated 1024×1024 CCD detector with a pixel size of $13.3 \times 13.3 \ \mu m^2$. The filter system is equipped with two narrow-band filters of 557.7 nm and 630.0 nm for OI airglow and a wide-band filter of 720–910 nm notched at 865 nm for OH airglow. With 2×2 binning of CCD, exposure times of 150 s and 20 s were used for the OI and OH airglow observation, respectively. The observing areas are estimated to be $600 \times 600 \ km^2$ for the OH airglow layer at 87 km, and $700 \times 700 \ km^2$ for the OI 557.7 nm airglow layer at 96 km. All images were digitized to 16-bit resolution in 512×512 pixel coordinates.

The airglow observation was carried out during moonless clear nights of March through October for years ranging 2008–2015. A total number of 1288 nights was observed during the eight years and monthly numbers are listed in Table 1. We adopted the method of Garcia et al. (1997) for image data reduction that includes background star removal and projection of the observed images into a flat airglow plane, making unwarped images. The unwarped images have spatial resolutions of 1.17 km/pixel for OH images and 1.37 km/pixel for OI-557.7 nm images. Wave events were selected as band type waves with the following criteria: (1) more than two wave crests span 13 (20%) out of 64 50 km×50 km square grids in the unwarped image, (2) the wave crests are separated farther than 10 km. A total number of 188 during 169 nights from OH images and 173 during 157 nights from OI-557.7 nm images were identified as wave events. Monthly numbers of wave events are presented in Table 1, which also tends to show greater rates of wave events during winter months due to longer observation hours than other months.

We adopted the method of Tang et al. (2005) to determine wave parameters of quasi-monochromatic waves using the two-dimensional (2-D) FFT algorithm. Before applying the 2-D FFT, three time-consecutive unwarped images (UI_{t+1}, UI_t, UI_{t-1}) were combined into two time-differenced images ($TD1=UI_t-UI_{t-1}$, $TD2=UI_{t+1}-UI_t$) by taking the difference of pixel intensities between two consecutive images.

Table 1
Monthly numbers of observed nights and wave events during the years of 2008–2015.

	Number of Observed Nights	Number of Wave events (OH Meinel bands)	Number of Wave events (OI 557.7)
March	161	13	19
April	135	27	29
May	157	29	28
June	149	42	28
July	172	26	24
August	169	35	27
September	158	13	15
October	141	3	3

Then we eliminated large-scale wave features from the time difference (TD) images using two-dimensional low-bandpass filter. The low-bandpass filter eliminates the spectral range smaller than 0.01 cycle/km (wavelengths larger than 100 km) from the FFT spectrum. The TD images show wave structures more clearly than the unwarped images, being ready for the FFT analysis. Applying 2-D FFT to two consecutive TD images, we obtained two complex arrays, $J_1(k, l)$ and $J_2(k, l)$, as functions of in zonal (k) and meridional (l) wavenumbers, and a cross spectrum defined as

$$f(k, l) = J_1(k, l)J_2^*(k, l) = R_1 R_2 \exp \ (i(\phi_1 - \phi_2)) \qquad (1)$$

where k and l are zonal and meridional wavenumbers, and R_1 and R_2 are the amplitudes, ϕ_1 and ϕ_2 are the phases of the two FFT arrays. The squared cross spectrum array, $|f(k, l)|^2$, indicates the power spectral density of the two TD images in the spatial frequency domain, and thus the maximum value of $|f(k, l)|^2$ corresponds to the strongest quasi-monochromatic wave component, called the dominant wave. The horizontal wavelength of the dominant wave was estimated from the maximum value position in the $|f(k, l)|^2$ array. Since no prominent secondary maximum position appears in the array, we are able to easily identify the dominant wave. The horizontal wavelength of the dominant wave was estimated from the horizontal wave number $k_h = (k^2 + l^2)^{1/2}$ corresponding to the dominant wave. The propagating direction of the dominant wave was determined from the ratio of zonal to meridional wavenumbers (k/l) of the maximum position with a 180° ambiguity. The ambiguity of propagating direction was resolved by examining the direction of the dominant wave propagation at the sequence of TD images as Tang et al. (2005) did. Since the phase difference between ϕ_1 and ϕ_2 in (1) occurred during the observed time difference Δt between the two TD images (typically Δt=318 s), one can estimate the observed horizontal phase speed $c_h = (\phi_2 - \phi_1)/k_h/\Delta t$. Finally, the period of the dominant wave was computed from the wavelength divided by the phase speed.

The derived wave parameters are in the ground reference system, but intrinsic properties of waves should be in the moving reference system with the background wind. For this, we used wind data simultaneously measured by a meteor radar (MR) at KSS. The KSS MR obtains wind information from radial velocities of radio echoes backscattered by meteor trails in the MLT region. The horizontal wind is routinely provided within a height-time sector of 2 km and 1 h in the 80–100 km altitude range. By adding the component of the horizontal wind in the direction of the observed phase speed we derive the intrinsic parameters. In addition, the KSS MR wind data allow us to calculate the vertical wind shear which affects wave propagation through the mesosphere.

Because the temperature structure is also vital in analyzing wave propagation especially in vertical direction, we utilized mesospheric temperatures over the KSS region ($-67.13°$S ± 10°, 57.13°W ± 10°) that were near-simultaneously measured by the Microwave Limb Sounder (MLS) on the Aura satellite (Waters et al., 2006).

3. Results and discussions

3.1. Observed wave parameters

Statistical distributions of observed wave parameters such as horizontal wavelength, observed phase speed, and observed period are shown in Fig. 1. The upper and lower plots indicate the observed wave parameters from OH Meinel band and OI-557.7 nm images, respectively. At both airglow layers the horizontal wavelengths are in the range of 10–50 km with typical values of 25–30 km. The observed phase speeds are between 8 and 85 m/s with majority being a relatively sharp peak at 20–25 m/s. The observed periods (derived from horizontal wavelength and observed phase speed) span from 5 to 60 min with dominant periods of 5–10 min at the OH layer and 15–20 min at
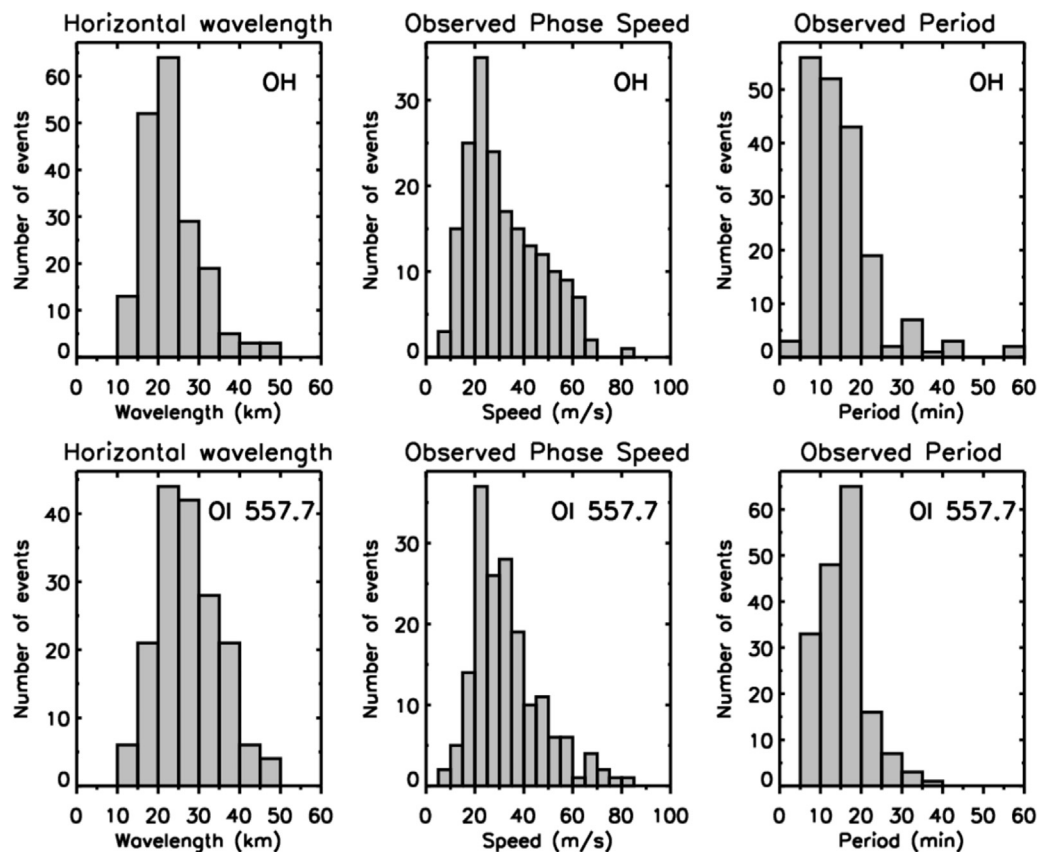
Fig. 1. Histograms of the horizontal wavelength (km), phase speed (m/s), and period (min) for band type waves obtained from OH and OI-557.7 nm airglow images.

the OI layer. The OH and OI airglow layers are known to be located at altitudes of 87 and 96 km, respectively (Taylor et al., 1997). These distributions of wave parameters are consistent with short period internal gravity waves, as indicated previous studies (e.g. Taylor et al., 1997; Hecht et al., 2001; Chung, 2005; Nielsen et al., 2009; Kim et al., 2010; Yang et al., 2015). Our analysis method can resolve waves with a phase speed faster than ~5 m/s (~distance for one pixel/time difference) and a wavelength smaller than 100 km (via low bandpass filter). Following the definition of short period gravity waves, we present the distribution of observed period only up to 1 h, which is well within the resolvable period.

The observed speeds and directions are shown as polar plots in the left panels of Fig. 2, where the length of each vector represents the propagation speed and direction (azimuth) of each wave event. The number of wave events that propagate within a 30° azimuth bin are presented in the right panels of Fig. 2. The observed wave speeds exhibit a strong anisotropy in such a way that westward waves are on average slower than eastward waves at both layers. The average speeds of the westward waves are 27.2 and 29.4 m/s for the OH and OI layers, respectively, while the corresponding speeds of the eastward waves are 44.2 and 46.1 m/s. However, westward propagating wave events are more common than eastward events. Given that majority of wave events were observed in wintertime, faster stratospheric winds may have filtered out efficiently eastward waves, thus allowing mostly westward waves to reach the mesosphere (Hines and Reddy, 1967; Taylor et al., 1993; Baumgaertner and McDonald, 2007; Wu et al., 2013). Vigorous orographic waves that are created by Southern Polar Vortex over the Antarctic Peninsula (Espy et al., 2006) may undergo critical filtering processes as the waves propagate upward to the MLT region. Accordingly, the strong anisotropy of westward propagating wave events may have occurred over KSS, which is located at Southern polar vortex boundary.

The seasonal variation of wave propagating headings observed at

KSS implies the rotating wave field over the Antarctic Peninsula, which was noticed by observations at neighboring stations, namely, Ferraz station (62.1°S, 58.4°W) and Rothera station (67°S, 68°W) (Espy et al., 2006; Bageston et al., 2009). The meridional component of wave propagating direction showed southward heading in wintertime, but northward heading in fall and spring. At Halley station (76°S, 27°W), located at the Antarctic continent, Nielsen et al. (2009) reported that the wave headings were persistently southward for all seasons, with a strong preference toward the south pole during winter. Probable sources of observed GWs over Halley were associated with strong cyclonic activity over Weddell Sea. The zonal components of waves headings observed at KSS tend to be strongly westward during winter and fall, and reversed to eastward in spring. During winter, the tendency of west propagating is characteristic over the Antarctic Peninsula and consistent with results from Rothera station (Espy et al., 2006). In this regard, Wu et al. (2013) reported that mesospheric zonal mean winds of the Antarctic Peninsula below 88 km were greatly affected by GWs during winter. Unlike Rothera station, a trend of eastward waves was observed at KSS during spring, implying that the underlying eastward wind fields are weaken more drastically over KSS than over Rothera. In fact, the difference in stratospheric winds between KSS and Rothera can be noted from a map of latitudinal-month variation of winds at 10 hPa in Waugh and Polvani (2010).

3.2. Intrinsic wave characteristics

The tendency that westward propagating waves show slower observed phase speed than eastward waves (Fig. 2) implies that the background wind in the MLT region over the Antarctic Peninsula is dominantly eastward. During winter, wind profiles measured by the KSS meteor radar (MR) were indeed predominantly eastward at the altitudes of 87 and 96 km, apparently causing westward waves to be slower than eastward waves observed in the all-sky images. At both
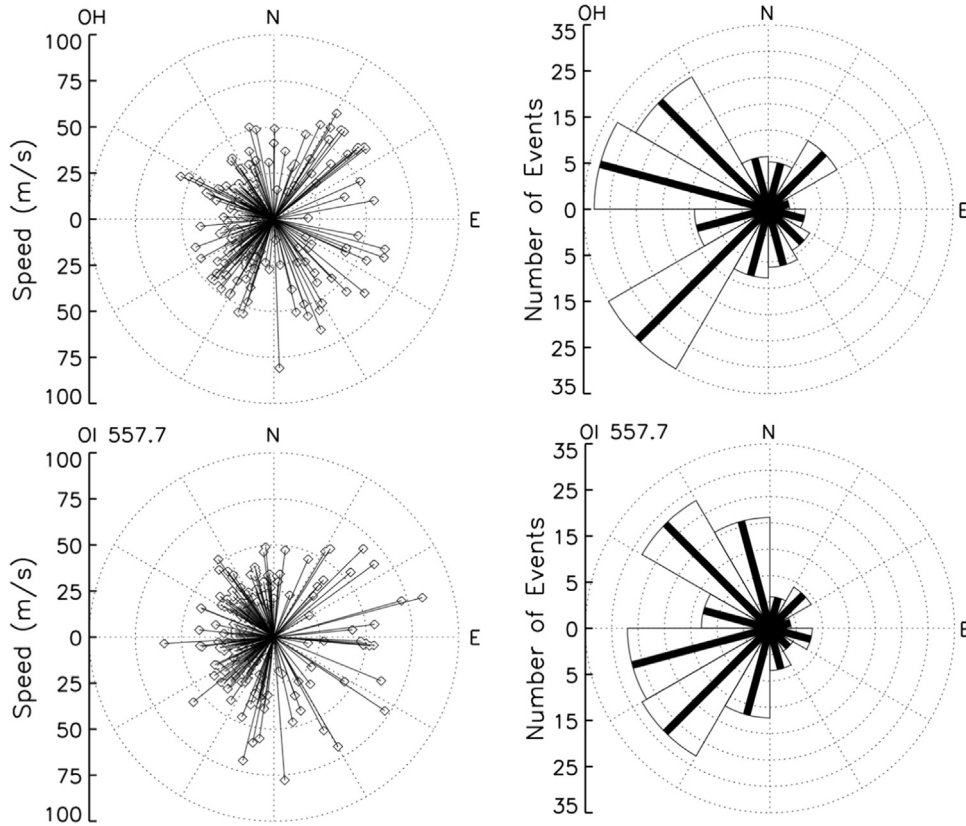
Fig. 2. Distributions of wave propagating directions and speeds (left) and the number of wave events (right) in each 30° azimuth bin at OH (top) and OI-557.7 nm (bottom) airglow layers.

altitudes (87 and 96 km), the majority of background winds blow eastward with maximum values of about 100 m/s at 87 km and 130 m/s at 96 km, respectively. Still in Fig. 2, the dominant and strong mesospheric eastward wind, determined from most of all-sky airglow imagers, is a well known climatology over the polar region during winter.

Using near-simultaneously (within an hour) measured MR winds, the intrinsic wave properties were determined for the 172 and 156 wave events in the OH and OI airglow layers, respectively. The intrinsic phase speed (c_{int}) is computed as $c_{int} = c - u$, using observed phase speed (c) and projected background wind (u) in the direction of wave propagation. The background wind is taken from the MR wind measured at the peak altitude, since the parameter of the dominant wave extracted from the airglow image reflects predominantly variation in airglow emission at the peak altitude, rather than the averaged variation over the airglow layer thickness (about 8 km). Wind changes over the layer thickness are less than 5 m/s, comparable to the uncertainty of observed phase speed. The observed phase period (τ_{int}) was estimated from intrinsic phase speed and observed horizontal wavelength (λ_h), using $\tau_{int} = \lambda_h/c_{int}$. Figs. 3 and 4 show polar plots of intrinsic phase speeds and histograms of intrinsic speeds and periods, respectively. Polar plots of the intrinsic waves show larger westward speeds, the opposite tendency to the observed waves due to the dominant eastward wind field (in comparison with Fig. 2). The intrinsic speeds are in the range of 2–140 m/s at the OH layer (87 km) and 1–130 m/s at the OI layer (96 km). The mean values of intrinsic phase speed are 54 m/s at 87 km and 48 m/s at 96 km, shifted from observed mean values of 32 m/s at 87 km and 33 m/s at 96 km. The shift is mostly due to strong eastward background winds that were subtracted. The distributions of intrinsic periods span from 5 to 60 min, dominant periods being 5–10 min and the mean values are 8 and 6 min at 87 and 96 km, respectively. The intrinsic periods are mostly shorter than the observed ones because of the opposite direction of the background

wind. The majority of intrinsic periods are between 5 min and 10 min, the typical value of mesospheric high-frequency GWs.

Fig. 5 presents polar histograms of the intrinsic periods, where radius indicates the magnitude of period with 1 min interval and the direction with a 10° azimuth bin. The inner and outer white dashed circles represent periods of 5 and 10 min, and thus most of the wave periods are in the range of 5–10 min. Southwest propagating waves (marked with red color in the plot) are dominant in both layers. The resemblance of both plots suggests that most waves may successively travel through both OH and OI airglow layers, thus vertical propagation.

3.3. Characteristics of vertical propagation

To characterize the vertical propagation of the observed waves, we utilize the above derived wave parameters and temperature profiles from MLS. As illustrated in previous studies (Isler et al., 1997; Nappo, 2002; Nielsen et al., 2012), the vertical wavenumber (m) of GWs can be derived from a simplified dispersion relation,

$$m^2 \approx \frac{N^2}{c_{int}^2} - \frac{1}{4H_s^2} - k^2 \tag{2}$$

where N is the Brunt-Väisälä (or buoyancy) frequency, H_s is the scale height, and k is the horizontal wavenumber ($2\pi/\lambda_h$). The buoyancy frequency and scale height were computed with temperatures measured on the same day by AURA/MLS.

The distributions of derived vertical wavelengths (λ_z) are shown in Fig. 6. The interquartile range of vertical wavelengths is 9–33 km with median values of 16 km and 15 km at the altitudes of 87 km and 96 km, respectively. The distributions are significantly different from those of Halley station, where the distribution at the altitude of 87 km (OH layer) ranges 16–48 km with a median vertical wavelength of 21 km (Nielsen et al., 2012). The difference is mainly due to the
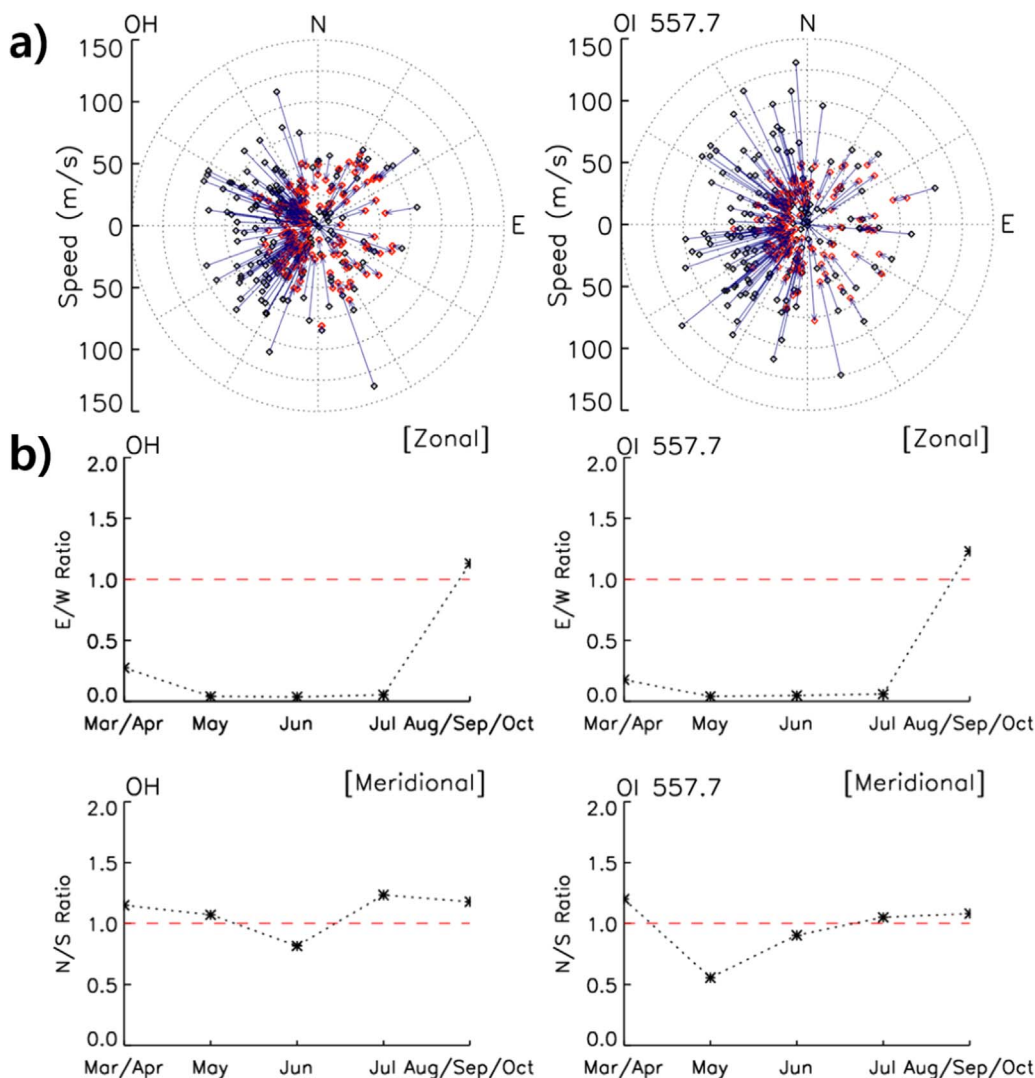
Fig. 3. a) Polar plots of intrinsic wave speeds (black) and observed speeds (red). The intrinsic wave speed was computed by subtracting the projected component of the background wind simultaneously measured by KSS meteor radar. b) Seasonal variations in the ratio of wave directions. (For interpretation of the references to color in this figure legend, the reader is referred to the web version of this article).

difference in Brunt-Väisälä frequencies that are determined by temperature structure, given that other parameters in Eq. (2) do not significantly contribute to the difference between two stations. Mesospheric temperatures tend to increase with latitudes during winter, so that lower temperatures over KSS lead to larger Brunt-Väisälä frequencies, resulting in smaller vertical wavelengths than those of Halley.

The characteristics of vertical propagation can be determined by examining the value of m^2 as a function of altitude. Fig. 7 shows sample profiles of m^2 to explain propagating types with an assumption that intrinsic wave parameters (c_{int} and k) at the OH layer stay constant over the altitudes. Three types of vertical propagation were suggested by previous studies (Isler et al., 1997; Nielsen et al., 2012). If m^2 is positive throughout the altitude range, the wave is freely propagating (Fig. 7a). If m^2 is negative throughout the altitudes, the wave propagates only horizontally, termed as evanescent waves (Fig. 7b). If a freely propagating region ($m^2 > 0$) is present and bounded by evanescent regions below and above (Fig. 7c), the wave is considered to be Doppler ducted. A Doppler ducted wave can be caused by favorable wind field, such as wind shear and curvature of the wind field. Especially, Doppler ducting is highly sensitive to the wave propagation direction against the background wind field and can allow waves to propagate long distances with little attenuation (Chimonas and Hines, 1986; Isler et al., 1997;

Hecht et al., 2001; Nielsen et al., 2012).

In addition to the above three types, we noted a case that a freely propagating region is present between 76 km and 98 km but not bounded by evanescent regions, the wave being ducted below or above a certain altitude (Fig. 7d). The partially ducted waves may be reflected at either top or bottom boundaries, and thus may affect the mesosphere horizontally in wider ranges than the freely propagating waves.

Using the wave parameters obtained from OH airglow images, we classified the vertical propagation types of 170 wave events, as listed in Table 2. The results excluded 18 wave events due to absence of either KSS MR wind data or MLS temperature data. We assumed the wave parameters form OH images unchanged in the process of vertical propagation. The freely propagating type was just less than a majority, while more than half the wave events had imaginary vertical wavenumbers in all or some altitudes between 76 and 98 km. According to Nielsen et al. (2012), the majority (80%) of wave events over Halley was the freely propagating type. The difference between KSS and Halley indicates that mesospheric GWs tend to propagate upward less freely in this part of the Antarctic Peninsula than over the Antarctic continent. This may imply that GWs may deposit their energy and momentum along the way more efficiently, thereby affecting mesospheric dynamics more over the Antarctic Peninsula than over the Antarctic continent.
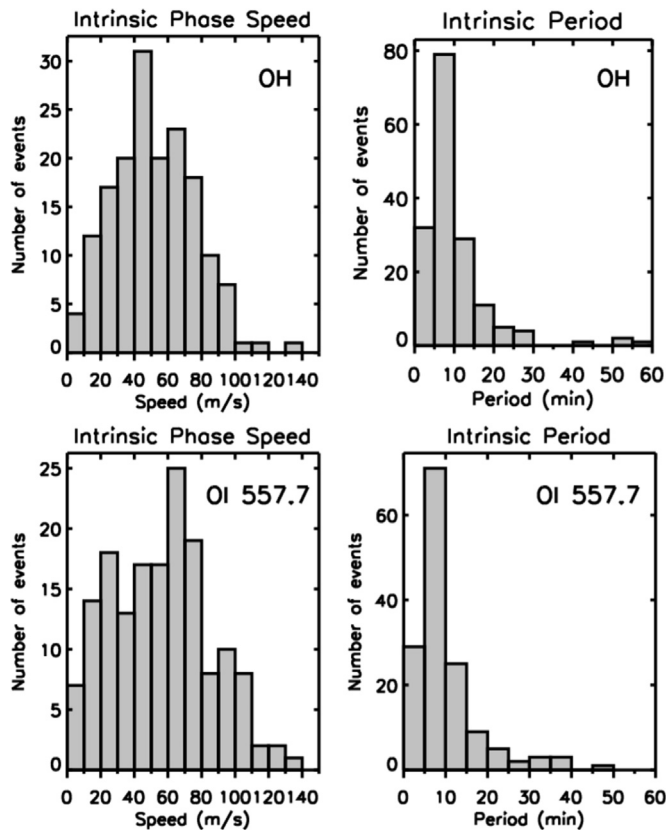
Fig. 4. Histograms of intrinsic phase speeds and periods for waves observed at OH (87 km) and OI 557.7 nm (96 km) airglow layers.

3.4. Comparison of waves between OH and OI airglow layers

In our observed wave events, waves were frequently detected in both images of OH Meinel bands and OI-557.7 nm. In order to analyze concurrent waves at both airglow layers, we applied the following four selection criteria. First, the wave structures should be observed at both layers during the same cycle of filter rotation. Second, the difference in observed horizontal wavelengths between two layers is less than 10 km. Third, propagating directions of waves should be within ± 15° of azimuthal angle at both layers. Fourth, the vertical wavenumber should be defined as freely propagating ($m^2 > 0$) at both layers. The second and third criteria were adopted in consideration of uncertainties in
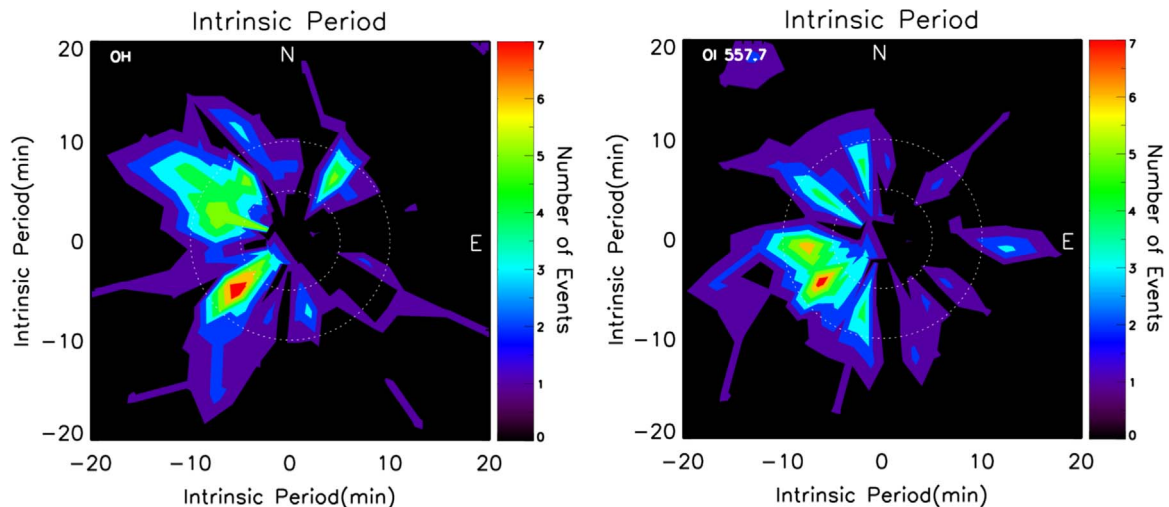

Fig. 6. Histograms of vertical wavelengths for waves observed at OH (87 km) and OI (96 km) airglow layers.

observed wavelengths and directions. With these criteria 19 wave events were selected as concurrent wave events at both layers during the 8 year's period of observation at KSS. We noted two types of concurrent wave events according to the difference in wave front angles between two layers, as illustrated in Fig. 8. The difference in front angles may imply wave refraction between two layers. The front angle can be estimated from the ratio of vertical wave number and horizontal wavenumber (m/k). For the case when the front angle at 87 km was larger than that of 96 km, we designated as 'Case 1′' events, and otherwise 'Case 2′'. The numbers of 'Case 1′' and 'Case 2′' were found to be 11 and 8, respectively.

Fig. 9 shows differences in wavenumbers (k, m) between the two layers, indicating that the difference in vertical wavenumber affects dominantly the front angle, thereby determining the case, rather than that in horizontal wavenumber. This is expected because we selected concurrent waves with similar horizontal wavelengths. If the vertical wavenumber increased (decreased) as GWs propagated from 87 km to 96 km, almost all the waves are in 'Case 1′' ('Case 2′') as marked with red (blue) stars. Thus the change of vertical wave number represents refraction of the wave.

In order to understand the wave refraction, we adopt the a ray tracing theory by Hasha et al. (2008), which explained a formulated three-dimensional ray-tracing scheme for internal GWs allowing wave refraction and horizontal propagation in spherical geometry. From Eq. (16) of Hasha et al. (2008), we simplified the change of vertical wavenumber along the ray as

Fig. 5. Polar histograms of intrinsic period for waves observed at OH (87 km) and OI (96 km) airglow layers. Inner white dash line circle means period of 5 min and outer white dash line circle means period of 10 min. (For interpretation of the references to color in this figure legend, the reader is referred to the web version of this article).
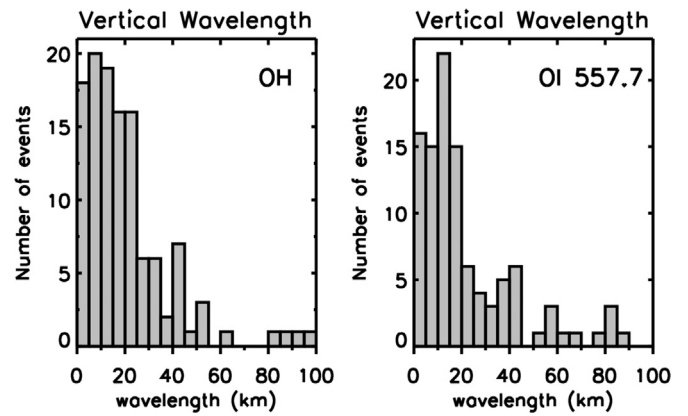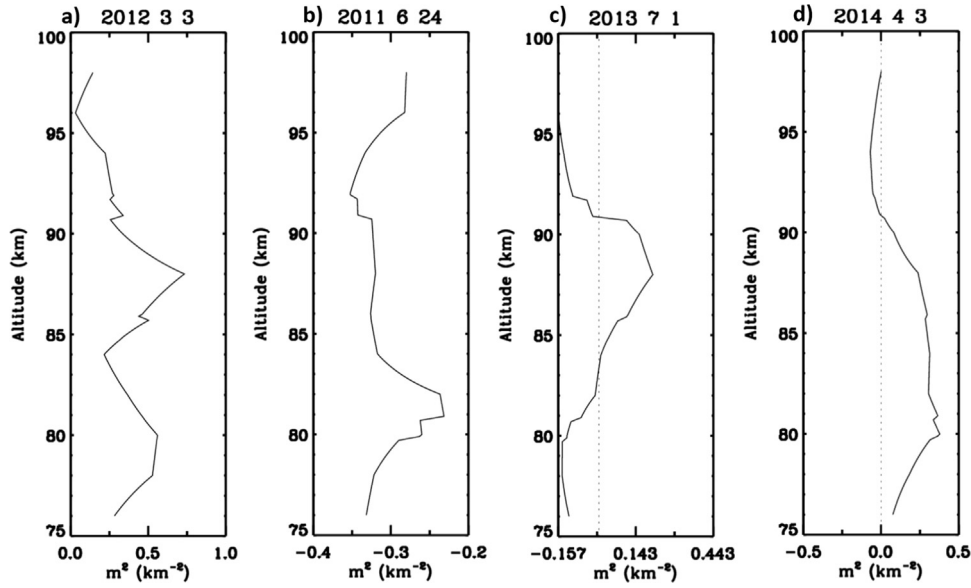
Fig. 7. Examples of squared vertical wavenumber profiles, a) freely propagating, b) evanescent, c) ducted, and d) partially ducted.

Table 2
Vertical propagating types observed at OH airglow layer (87 km) during the 8 year period at KSS.

Vertical propagating type	Number of events (Percentage)
Freely Propagating	78 (46%)
Evanescent	3 (2%)
Doppler Ducted	35 (20%)
Partially Ducted	54 (32%)

$$\frac{d|m|}{dt} \approx |k|\left[\frac{du}{dz} - \frac{|k|}{2\hat{\omega}\Delta}\frac{\partial N^2}{\partial z}\right] \quad (3)$$

where $\hat{\omega}$ is frequency of GWs, Δ is equal to $k^2+m^2+\alpha^2$, and $\alpha = -0.5\rho^{-1}\partial\rho/\partial z$, ρ being atmospheric density. In derivation of the simplified Eq. (3), the term with Coriolis frequency was neglected because of much large values in high frequency GWs, and the mesospheric GWs were assumed to be propagating only upward (Tsuda, 2014). The term, $\frac{du}{dz}$ means vertical wind shear, and $\frac{\partial N^2}{\partial z}$ indicates the gradient of squared Brunt-Väisälä frequency that is proxy for the background stability condition. Although the gradient of squared Brunt-Väisälä frequency has significantly negative values around 90–92 km near the temperature inversion altitudes, similar conditions

occurred for both 'Case 1′' and 'Case 2′'. However, the vertical wind shear was quite different between 'Case 1′' and 'Case 2′', hence indicating a critical factor. Wave events of 'Case1′' were found to be associated with mostly positive wind shear, whereas the 'Case 2′' events were with negative wind shear. Specifically, the change of vertical wavenumber for 'Case 1′' and 'Case 2′', as in Eq. (3), is caused by negative and positive contribution of integrated wind shear over 87–96 km, respectively. Therefore, the wind shear is the main factor in wave refraction that was estimated from the difference in wave front angles between 87 km and 96 km, given that similar atmospheric stability conditions prevailed over the Antarctic Peninsula.

4. Summary and conclusions

We have analyzed all-sky airglow images observed with OH Meinel band and OI-557.7 nm filters at KSS during the period of 2008–2015. By applying 2-dimensional FFT to time differenced images, we found a total of 188 and 173 wave events in the OH and OI images, respectively. The observed waves were predominantly westward, implying that eastward waves were filtered out by strong eastward winds in the intermediate atmosphere over KSS. Unlike the neighboring Rothera station, a trend of eastward waves was found during spring time, which is consistent with the stratospheric wind pattern, wherein
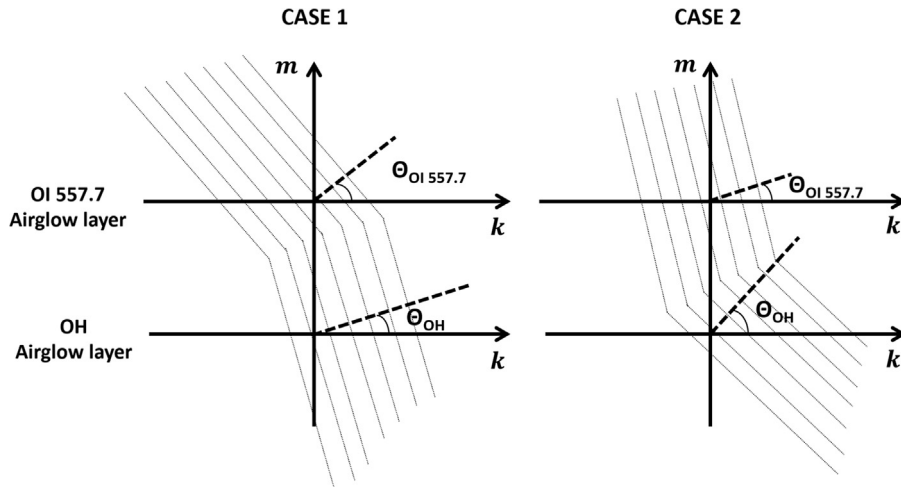

Fig. 8. Two cases of wave front angles between two layers.
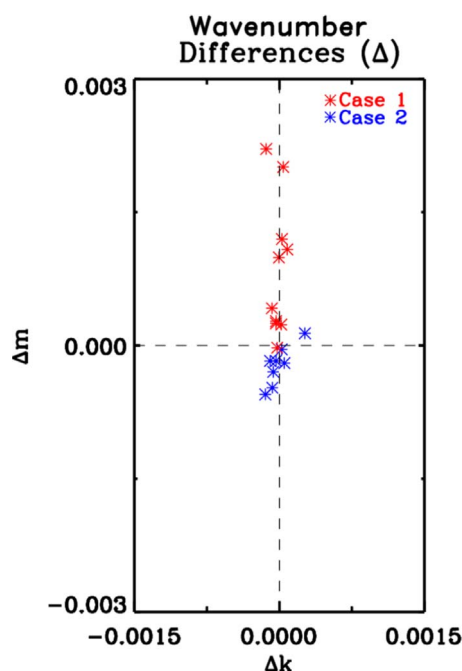
Fig. 9. Differences in horizontal and vertical wavenumbers between two layers. The x and y-axis represent differences in horizontal wavenumber (k) and vertical wavenumber (m). The red and blue symbols indicate Case 1 and Case 2, respectively. (For interpretation of the references to color in this figure legend, the reader is referred to the web version of this article).

the eastward wind fields are weaken more drastically over KSS than over Rothera. Utilizing background winds simultaneously measured by KSS meteor radar and MLS temperatures, we derived intrinsic wave parameters and vertical wavenumbers. The distributions of intrinsic wave parameters, namely phase speed and phase period, are consistent with mesospheric short-period GWs, as in previous studies over Antarctica. More than half of the wave events were vertically evanescent or Doppler ducted (~54%), which might be due to strong eastward background wind in the mesosphere over KSS. For freely propagating waves, the vertical wavelengths were in the interquartile range of 5–35 km with a median value of 15 km. The vertical wavelengths are shorter than those observed at Halley station, where the majority of the observed waves were freely propagating (Nielsen et al., 2012). The difference in the wave propagating characteristics between KSS and Halley suggests that GWs may deposit energy and momentum along the way more efficiently, thereby affecting mesospheric dynamics more in this part of the Antarctic Peninsula than over the Antarctic continent. Finally, we estimated the changes in vertical and horizontal wavenumbers between OH and OI layers, as a proxy of wave refraction. According to the ray tracing theory by Hasha et al. (2008), the large wind shear observed over KSS is the main cause of the GWs refraction among other physical parameters. Therefore, not only the mean wind but also the wind shear plays an important role in vertical wave propagation over the Antarctic Peninsula.

Acknowledgements

References

Alexander, M.J., Gille, J., Cavanaugh, C., Coffey, M., Craig, C., Eden, T., Francis, G., Halvorson, C., Hannigan, J., Khosravi, R., Kinnison, D., Lee, H., Massie, S., Nardi, B., Barnett, J., Hepplewhite, C., Lambert, A., Dean, V., 2008. Global estimates of gravity wave momentum flux from high resolution dynamics limb sounder (HIRDLS) observations. J. Geophys. Res. 113, (D15S18).

Alexander, M.J., Teitelbaum, H., 2007. Observation and analysis of a large amplitude mountain wave event over the Antarctic peninsula. J. Geophys. Res. 112, D21103.

Bageston, J.V., Wrasse, C.M., Gobbi, D., Takahashi, H., Souza, P.B., 2009. Observation of mesospheric gravity waves at Comandante Ferraz Antarctica Station (62°S). Ann. Geophys. 27, 2593–2598.

Baumgaertner, A.J.G., McDonald, A.J., 2007. A gravity wave climatology for Antarctica compiled from challenging minisatellite payload/global positioning system (CHAMP/GPS) radio occultations. J. Geophys. Res. 112 (D5), D05103.

Chimonas, G., Hines, C.O., 1986. Doppler ducting of atmospheric gravity waves. J. Geophys. Res. 91, 1219–1230.

Chung, J.K., 2005. Observation of Upper Atmospheric Phenomena With Ground-based Instruments (Ph.D. Dissertation). Chungnam National University, Daejeon, Korea.

Ern, M., Preusse, P., Alexander, M.J., Warner, C.D., 2004. Absolute values of gravity wave momentum flux derived from satellite data. J. Geophys. Res. 109, D20103.

Espy, P.J., Hibbins, R.E., Swenson, G.R., Tang, J., Taylor, M.J., Riggin, D.M., Fritts, D.C., 2006. Regional variations of mesospheric gravity wave momentum flux over Antarctica. Ann. Geophys. 24, 81–88.

Espy, P.J., Jones, G.O.L., Swenson, G.R., Tang, J., Taylor, M.J., 2004. Seasonal variations of the gravity wave momentum flux in the Antarctic mesopause and lower thermosphere. J. Geophys. Res. 109, D23109.

Fritts, D.C., Alexander, M.J., 2003. Gravity wave dynamics and effects in the middle atmosphere. Rev. Geophys. 41 (1).

Fritts, D.C., Vincent, R.A., 1987. Mesospheric momentum flux studies at Adelaide, Australia: observations and a gravity wave/tidal interaction model. J. Atmos. Sci. 44 (3), 605–619.

Garcia, J.K., Taylor, M.J., Kelley, M.C., 1997. Two-dimensional spectral analysis of mesospheric airglow image data. Appl. Opt. 36 (29), 7374–7385.

Gavrilov, N.M., Shved, G.M., 1982. Study of internal gravity waves in the lower thermosphere from observations of the nocturnal sky airglow [OI] 5577 Å in Ashkhabad. Ann. Geophys. 38 (6), 789–803.

Gavrilov, N.M., Shiokawa, K., Ogawa, T., 2002. Seasonal variations of medium-scale gravity wave parameters in the lower thermosphere obtained from spectral airglow temperature imager observations at Shigaraki, Japan. J. Geophys. Res. 107 (D24), 4755.

Hasha, A., Buhler, O., Scinocca, J., 2008. Gravity wave refraction by three-dimensionally varying winds and the global transport of angular momentum. J. Atmos. Sci. 65, 2892–2906.

Hecht, J.H., Walterscheid, R.L., Hickey, M.P., Franke, S.J., 2001. Climatology and modeling of quasi-monochromatic atmospheric gravity waves observed over Urbana Illinois. J. Geophys. Res. 106 (D6), 5181–5195.

Hertzog, A., Boccara, G., Vincent, R.A., Vidal, F., Cocquerez, P., 2008. Estimation of gravity wave momentum flux and phase speeds from quasi-Lagrangian stratospheric baloon flight. Part II: results from the Vorcore campaign in Antarctica. J. Atmos. Sci. 65, 3056–3070.

Hines, C.O., Reddy, C.A., 1967. On the propagation of atmospheric gravity waves through regions of wind shear. J. Geophys. Res. 72, 1015–1034.

Isler, J.R., Taylor, M.J., Fritts, D.C., 1997. Observational evidence of wave ducting and evanescence in the mesosphere. J. Geophys. Res. 102 (22), 301–313.

Jiang, J.H., Wu, D.L., Eckermann, S.D., Ma, J., 2003. Mountain waves in the middle atmosphere: microwave limb sounder observations and analyses. Adv. Space Res. 32 (5), 801–806.

Kim, Y.H., Lee, C., Chung, J.K., Kim, J.H., Chun, H.Y., 2010. Seasonal variations of mesospheric gravity waves observed with an airglow all-sky camera at Mt. Bohyun, Korea (36°N). J. Astron. Space Sci. 27, 181–188.

Krassovski, V., 1972. Infrasonic variations of OH emission in the upper atmosphere. Ann. Geophys. 28, 739–746.

Lee, C., Kim, Y.H., Kim, J.H., Jee, G., Won, Y.I., Wu, D.L., 2013. Seasonal variation of wave activities near the mesopause region observed at King Sejong Station (62.22°S, 58.78°W), Antarctica. J. Atmos. Sol.-Terr. Phys. 105–106, 30–38.

Moffat-Griffin, T., Hibbins, R.E., Jarvis, M.J., Colwell, S.R., 2011. Seasonal variations of gravity wave activity in the lower stratosphere over an Antarctic Peninsula station. J. Geophys. Res. 116, D14111.

Nappo, C.J., 2002. An introduction to atmospheric gravity waves 85. Academic, International Geophysics Series, San Diego, Calif.

Nielsen, K., Taylor, M.J., Hibbins, R.E., Jarvis, M.J., 2009. Climatology of short-period mesospheric gravity waves over Halley, Antarctica (76°S, 27°W). J. Atmos. Sol.-Terr. Phys. 71, 991–1000.

Nielsen, K., Taylor, M.J., Hibbins, R.E., Jarvis, M.J., Russell, J.M., III, 2012. On the nature of short-period mesospheric gravity wave propagation over Halley, Antarctica. J. Geophys. Res. 117, D05124.

Plougonven, R.A., Teitelbaum, H., 2008. Observations and simulations of a large-amplitude mountain wave breaking over the Antarctic Peninsula. J. Geophys. Res. 113, D16113.

Smith, A.K., 2004. Physics and chemistry of the mesopause region. J. Atmos. Sol.-Terr. Phys. 66 (10), 839–857.

Swenson, G.R., Mende, S.B., 1994. OH emission and gravity waves (including a breaking wave) in all-sky imagery from Bear Lake, UT. Geophys. Res. Lett. 21 (20), 2239–2242.

Tang, J., Kamalabadi, F., Franke, S.J., Liu, A.Z., Swenson, G.R., 2005. Estimation of gravity wave momentum flux with spectroscopic imaging. IEEE Trans. Geosci. Remote Sens. 43 (1), 103–109.

Taylor, M.J., Hapgood, M.A., Rothwell, P., 1987. Observations of gravity wave propagation in the OI (557.7 nm), Na (589.2 nm) and the near infrared OH nightglow emissions. Planet. Space Sci. 35 (4), 413–427.

Taylor, M.J., Bishop, M.B., Taylor, V., 1995a. All-sky measurements of short period waves imaged in the OI(557.7 nm), Na(589.2 nm) and near infrared OH and O2(0,1) nightglow emissions during the ALOHA-93 campaign. Geophys. Res. Lett. 22 (20), 2833–2836.

Taylor, M.J., Gu, Y.Y., Tao, X., Gardner, C.S., Bishop, M.B., 1995b. An investigation of intrinsic gravity wave signatures using coordinated lidar and nightglow image measurements. Geophys. Res. Lett. 22 (20), 2853–2856.

Taylor, M.J., Pendleton, W.R., Jr., Clark, S., Takahashi, H., Gobbi, D., Goldberg, R.A., 1997. Image measurements of short-period gravity waves at equatorial latitude. J. Geophys. Res. 98 (A4), 6047–6057.

Taylor, M.J., Ryan, E.H., Tuan, T.F., Edwards, R., 1993. Evidence of preferential directions for gravity wave propagation due to wind filtering in the middle atmosphere. J. Geophys. Res. 98, 6047.

Tsuda, T., 2014. Characteristics of atmospheric gravity waves observed using MU (Middle and Upper atmosphere) radar and GPS (Global Positioning System) radio occultation. In: Proceedings of the Japan Academy Ser B Physical and Biological Sciences. 90(1), pp. 12–27.

Waters, J.W., Froidevaux, L., Jarnot, R.F., Pickett, H.M., Read, W.G., Siegel, P.H., Cofield, R.E., Flower, D.A., Holden, J.R., Lau, G.K., Livesey, N.J., Manney, G.L., Santee, M.L., Wu, D.L., Cuddy, D.T., Lay, R.R., Loo, M.S., Perun, V.S., Schwartz, M.J., Stek, P.C., Thurstans, R.P., Boyles, M.A., Chandra, K.M., Chavez, M.C., Chen, G.S., Chudasama, B.V., Dodge, R., Fuller, R.A., Girard, M.A., Jiang, J.H., Jiang, Y., Knosp, B.W., LaBelle, R.C., Lam, J.C., Lee, K.A., Miller, D., Oswald, J.E., Patel, N.C., Pukala, D.M., Quintero, O., Scaff, D.M., Van Snyder, W., Tope, M.C., Wagner, P.A., Walch, M.J., 2006. The earth observing system microwave limb sounder (EOS MLS) on the aura satellite. IEEE Trans. Geosci. Remote Sens. 44 (5), 1075–1092.

Waugh, D.W., Polvani, L.M., 2010. Stratospheric Polar Vortices. In: Polvani, L.M., Soble, A.H., Waugh, D.W. (Eds.), The Stratosphere: Dynamics, Transport, and Chemistry 190. American Geophysical Union, Geophysical Monograph Series, Washington D.C, 43–57.

Wu, D.L., Jiang, J.H., 2002. MLS observations of atmospheric gravity waves over Antarctica. J. Geophys. Res. 107 (D24), 4773.

Wu, D.L., Eckermann, S.D., 2008. Global gravity wave variances from Aura MLS: characteristics and interpretation. J. Atmos. Sci. 65, 3695–3718.

Wu, Q., Chen, Z., Mitchell, N., Fritts, D.C., Iimura, H., 2013. Mesospheric wind disturbances due to gravity waves near the Antarctica Peninsula. J. Geophys. Res. 118, 7765–7772.

Yang, T.Y., Kwak, Y.S., Kim, Y.H., 2015. Statistical comparison of gravity wave characteristics obtained from airglow all-sky observation at Mt. Bohyun, Korea and Shigaraki, Japan. J. Astron. Space Sci. 32 (4), 327–333.

Yoshiki, M., Kizu, N., Sato, K., 2004. Energy enhancements of gravity waves in the Antarctic lower stratosphere associated with variations in the polar vortex and tropospheric disturbances. J. Geophys. Res. 109, D23104.